Hardware-In-The-Loop Simulation of a Heaving Wave Energy Converter

Chris D. Signorelli[#1], Carlos Villegas[#2], John V. Ringwood[*3]

[#]*Wavebob Ltd, H3 Maynooth Business Campus, Co. Kildare, Ireland*

[1] chris.signorelli@wavebob.com

[2]carlos.villegas@wavebob.com

[*]*Department of Electronic Engineering, National University of Ireland, Maynooth*

[3]john.ringwood@eeng.nuim.ie

Abstract— **The technical challenges in developing PTO systems for wave energy converters are enormous as they have to accommodate both power absorption and survival of extreme waves. The design of PTO systems and their controllers requires complex simulations, taking into account the interaction with the wave energy converter (WEC). However, many of the properties for continuous operation are difficult to reproduce in simulation. PTO and control design for WECs can be facilitated using onshore hardware-in-the-loop (HIL) test-rigs. By performing HIL simulations, it is possible to test the actual PTO and its control equipment under typical operating conditions. To demonstrate the concept we have adapted the scale model of a two degree-of-freedom heaving point-absorber to be tested in this manner. To recreate typical operating conditions, we created and validated a real-time simulation of the WEC, enabling its motion to be emulated using a hydraulic prime mover. The degree of novelty with this work concerns the application of HIL to the above WEC, with real hardware, using an emulated pan-chromatic sea-state. Experimental results demonstrate the effectiveness of the approach to test a representative PTO system.**

Keywords— **Hardware in the loop, wave energy, power take-off, point absorber, state space, Prony.**

I. NOMENCLATURE

t = Time (s).
k = Index for each angular frequency of the sea-state.
A_k = Wave elevation of the *k*-th angular frequency component of the sea-state (m).
ω_k = *k*-th angular frequency of the sea-state (rad.s^{-1}).
$S(\omega_k)$ = *k*-th element of the wave elevation spectral density function (m^{2}s.rad^{-1}).
ω = Angular frequency (rad.s^{-1}).
$d\omega$ = Angular frequency step size (rad.s^{-1}).
H_s = Significant wave height of sea-state (m).
T_p = Peak period of sea-state (s).
γ = Gamma parameter used for JONSWAP sea-state spectrum.
$\psi_1(t)$ = Heave position of WEC body-1 relative to the still water datum (m).
$\psi_2(t)$ = Heave position of WEC body-2 relative to the still water datum (m).
$\dot{\psi}_1(t)$ = Heave velocity of body-1 (m.s^{-1}).
$\dot{\psi}_2(t)$ = Heave velocity of body-2 (m.s^{-1}).
$\ddot{\psi}_1(t)$ = Heave acceleration of body-1 (m.s^{-2}).
$\ddot{\psi}_2(t)$ = Heave acceleration of body-2 (m.s^{-2}).
$\psi_{rel}(t)$ = Relative position of both bodies (m).
$\dot{\psi}_{rel}(t)$ = Relative velocity of both bodies (m.s^{-1}).
m_1 = Mass of body-1 (kg).
m_2 = Mass of body-2 (kg).
$a_{\infty_{11}}$ = Added mass at infinite frequency of body-1 (kg).
$a_{\infty_{12}}$ = $a_{\infty_{21}}$ = Added mass at infinite frequency due the interaction of both bodies (kg).
$a_{\infty_{22}}$ = Added mass at infinite frequency of body-2 (kg).
$L_{11}(t)$ = Impulse response function of body-1 (N.m^{-1}).
$L_{12}(t)$ = $L_{21}(t)$ = Impulse response function due the interaction of both bodies (N.m^{-1}).
$L_{22}(t)$ = Impulse response function of body-2 (N.m^{-1}).
c_1 = Hydrostatic stiffness of body-1 (N.m^{-1}).
c_2 = Hydrostatic stiffness of body-2 (N.m^{-1}).
$f_{e_1}(t)$ = Excitation force acting on body-1 (N).
$f_{e_2}(t)$ = Excitation force acting on body-2 (N).
$f_{PTO}(t)$ = PTO force (N).
$\mathbf{X}(t)$ $\in \mathbb{R}^{n\,x\,1}$ = State variable for overall state space WEC model.
$\dot{\mathbf{X}}(t)$ $\in \mathbb{R}^{n\,x\,1}$ = Time derivative of $\mathbf{X}(t)$.
$x_1(t)$ = $\dot{\psi}_1(t)$ = State variable 1 of $\mathbf{X}(t)$.
$x_2(t)$ = $\dot{\psi}_2(t)$ = State variable 2 of $\mathbf{X}(t)$.
$x_3(t)$ = $\psi_1(t)$ = State variable 3 of $\mathbf{X}(t)$.
$x_4(t)$ = $\psi_2(t)$ = State variable 4 of $\mathbf{X}(t)$.
$\mathbf{A}$ $\in \mathbb{R}^{n\,x\,n}$ = State matrix for overall state space WEC model.
$\mathbf{B}$ $\in \mathbb{R}^{n\,x\,r}$ = Input matrix for overall state space WEC model.
$\mathbf{C}$ $\in \mathbb{R}^{m\,x\,n}$ = Output matrix for overall state space WEC model.
$\mathbf{D}$ $\in \mathbb{R}^{m\,x\,r}$ = Direct transmission matrix for overall state space WEC model.
$\mathbf{F}(t)$ $\in \mathbb{R}^{r\,x\,1}$ = Control matrix for overall state space WEC model, including excitation and PTO forces (N).
$y(t)$ = $\psi_{rel}(t)$ = Output of overall state space WEC model (m).
DoF = Degrees of freedom used for WEC model.

$\mathbf{M}$ $\in \mathbb{R}^{\mathrm{DoF\,x\,DoF}}$ = Mass matrix (kg).
$\mathbf{K}$ $\in \mathbb{R}^{\mathrm{DoF\,x\,DoF}}$ = Hydrostatic stiffness matrix (N.m^{-1}).
$\mathbf{I}$ $\in \mathbb{R}^{\mathrm{DoF\,x\,DoF}}$ = Identity matrix.
$\mathbf{X}_{\mathrm{C}}(t)$ $\in \mathbb{R}^{p\,\mathrm{x}\,1}$ = State variable for convolution integral approximations.
$\dot{\mathbf{X}}_{\mathrm{C}}(t)$ $\in \mathbb{R}^{p\,\mathrm{x}\,1}$ = Time derivative of $\mathbf{X}_{\mathrm{C}}(t)$.
$\mathbf{A}_{\mathrm{C}}$ $\in \mathbb{R}^{p\,\mathrm{x}\,p}$ = State matrix for convolution integral approximations.
$\mathbf{B}_{\mathrm{C}}$ $\in \mathbb{R}^{p\,\mathrm{x}\,1}$ = Input matrix for convolution integral approximations.
$\mathbf{C}_{\mathrm{C}}$ $\in \mathbb{R}^{1\,\mathrm{x}\,p}$ = Output matrix for convolution integral approximations.
$L(t)$ = Arbitrary impulse response function (N.m^{-1}).
$\hat{L}(t)$ = Resampled $L(t)$, evenly spaced (N.m^{-1}).
Q = Number of complex damped sinusoidal components of $\hat{L}(t)$ used in approximation.
i = Index for each complex damped sinusoid of $\hat{L}(t)$.
A_i = Amplitude of *i*-th complex damped sinusoid of $\hat{L}(t)$.
σ_i = Damping factor of *i*-th complex damped sinusoid of $\hat{L}(t)$.
ω_i = Angular frequency of *i*-th complex damped sinusoid of $\hat{L}(t)$.
ϕ_i = Phase of *i*-th complex damped sinusoid of $\hat{L}(t)$.
$\hat{L}_i$ = *i*-th complex damped sinusoid of $\hat{L}(t)$.
s = Laplace domain complex variable.
$v_b(t)$ = Velocity of 'body-*b*' in the time domain. Note 'body-*b*' could be body-1 or body-2.
$V_b(s)$ = Velocity of 'body-*b*' in the frequency domain.
$Y_{C_i}(s)$ = Laplace domain output of the *i*-th component of the convolution integral approximation.
$x_{1c_i}(t)$ = State variable 1 of $\mathbf{X}_{\mathrm{C}}(t)$.
$x_{2c_i}(t)$ = State variable 2 of $\mathbf{X}_{\mathrm{C}}(t)$.
$\dot{x}_{1c_i}(t)$ = Time derivative of x_{1c_i}.
$\dot{x}_{2c_i}(t)$ = Time derivative of x_{2c_i}.

II. Introduction

Wave energy developers face significant challenges when attempting to deploy sea-going WECs. Onshore testing of large scale PTOs is often simplistic in nature and tends not to cater for realistic sea conditions, preventing WEC developers gaining a complete understanding of the dynamics of their large scale devices, pre-deployment. This leads to increased risk, over-engineering, design complexity and sub-optimal power capture performance.

The design of PTO systems and their controllers can benefit from the use of complex simulations, taking into account interaction with the WEC. However, many of the properties for continuous operation such as hydraulic fluid degradation or system faults are difficult to reproduce in simulation. Another disadvantage of this approach is the reliance on many simplifying assumptions, adopted either for the purpose of model simplicity or computational efficiency. Although these simplifications facilitate the use of well established analysis techniques they also give rise to model inaccuracies. For example, effects often neglected in hydraulic PTOs are cylinder friction, valve stiction and oil compressibility. From the point of view of PTO modelling, system saturation constraints on force, velocity and power are often omitted as they introduce inconvenient nonlinearities, presenting difficulties for linear analysis techniques.

Wave tank testing has the benefit of removing many of these simplifications where scaled models are built and subjected to approximated sea states, usually uni-directional, in wave tank basins. However it is impossible to use large sea going devices due to the size restrictions of the wave tank facility and therefore, the scale PTO is only *representative* of that to be used at sea. While wave tank testing removes many of the simplifications associated with computer simulations, specialist expertise is required from wave tank operators, divers and test equipment technicians. Availability is also difficult due to high demand across several marine industries. Another consideration regarding the use of representative PTOs in wave tank testing is that design conflicts can arise due to the different scaling laws of the various components. For example Froude scaling of hydrodynamic parameters relies on the ratio of inertia or pressure forces to gravity and not Reynold's number, whereas hydraulic machines do scale according to Reynold's number [1].

PTO and control design for wave energy converters can be facilitated using onshore hardware-in-the-loop test-rigs. By using HIL simulation, it is possible to test the actual PTO and its control equipment under typical operating conditions. It is suggested here that the HIL approach can complement computer simulations and wave tank testing to achieve more realistic test conditions of large scale PTOs, pre-deployment. It is envisaged that tank testing would provide precise hydrodynamic data, on the basis of which accurate mathematical models could be formed and then used on onshore HIL test rigs. Wave tank testing would be simplified, only requiring installation of representative small scale PTOs without consideration of the specific details of the large scale PTO technology.

This paper is presented as follows: Section III gives a state-of-the-art review of HIL across other application areas and also its documented use within the wave energy field; Section IV provides an overall system description of the HIL test-rig composition, outlining the real versus simulated parts, the treatment of excitation forces and a detailed description of each main HIL component; Section V provides details of the PTO and section VI explains the WEC's hydrodynamic state space model; Section VII explains the hardware and software architecture of the HIL system; Section VIII provides a discussion of the experimental results, following which the conclusions are presented.

III. Hardware-in-the-Loop Perspectives

HIL began its development in the early 20th century, initially being used as an alternative to full system deployment and later as an alternative to computer simulations, where some processes are real and others simulated [2]. The decision of which processes are real or simulated is dictated by the individual requirements of the application. The success of HIL

has resulted in wide-spread use across several industries and is reported to have the following advantages [2]:

- Mathematical models of some systems and therefore their software models can be difficult to obtain;
- The characteristics of sensors and actuators are seldom available to an adequate level, some examples being noise, deadband, hysteresis and backlash;
- Design and testing of control systems is made possible without the need to operate in the real environment;
- Testing of the control hardware and software may be required for extreme conditions in a laboratory environment such as high temperatures, high acceleration, shock or electro-magnetic compatibility;
- Testing system behaviour in the presence of fault conditions of actuators, sensors and control algorithms is made possible;
- Time and cost savings can be made when prototyping.

A. HIL Application Areas Outside Wave Energy

Engine control systems have been tested using HIL in [2] for two particular series of Mercedes trucks where the main purpose was to record the engine and vehicle subsystem responses under injection pump fault conditions. The simulated parts of the system were the engine dynamics, turbo charger and vehicle drive train. The real parts were the vehicle-engine control unit, pump-line-nozzle control unit and injection pumps. During the HIL simulations individual injection pumps were switched off, simulating operational faults.

Rail vehicle control systems have been tested in [3] with the purpose of evaluating a digital HIL simulator for line-converter controlled rail vehicles where previously most testing was done using analog technology. The simulated components of the system consist of converters, filters, drives, and mechanics representing the electro-mechanics of the vehicle. The real components were the locomotive control system, wheel-rail contact, and electrical network. It was found, while considering the system's fast dynamics and discrete handling of causality changes, that a significant amount of processing power and careful use of numeric solvers was required when attempting HIL simulation. It was also commented that the HIL simulations simplified track tests upon vehicle rollout.

HIL has been applied to a space robot control system in [4] that was aimed at using HIL to assist in the verification of all tasks of a special purpose dextrous manipulator (SPDM) for use at the international space station. The simulated part of the system was the space hardware as it could not support its own weight on earth. The real component was a ground based robot used to emulate the contact forces between the manipulator and complex objects where a lack of adequate mathematical models prevented the use of computer simulations. The outcome of the project was the successful control of the ground robot using HIL while mimicking the dynamic behaviour of the SPDM. HIL simulation also allowed for the trial of two independent control algorithms, providing insight into their relative performance and stability characteristics.

Machine tool chatter has been investigated using HIL in [5] to facilitate the analysis of instability in regenerative machine-tool-chattering, extremely difficult to achieve on real machines [5]. The simulated components of the HIL loop were the cutting force and cutting delay, with the delay simulating the time between successive passes of the tool over the same radial position of the rotating shaft. The real component was a metal beam upon which the cutting force and delay were emulated using a voice coil. Instability was reproduced for certain combinations of simulation parameters, after which a specialised damping strategy was designed to stabilise the system.

HIL has been used on a wind turbine R&D platform in [6] to help evaluate a large-scale HIL test rig, previously used for ship propulsion systems, while trialling a novel control strategy for small-scale wind energy systems. The simulated components of the system were: a neural network for estimating the wind velocity profile; a maximum power tracking algorithm; and the wind turbine dynamics. The real component of the system was a 15kW motor-generator used to emulate the turbine shaft torque and angular speed. It was found that the 'maximum-tracking' control algorithm worked well and that even while running at 50uS sample rate the controller was underutilised. It was therefore concluded that there exists the potential for more advanced control algorithms to be tested on the proposed HIL test rig following an expansion of the generator control unit.

B. HIL in Wave Energy

There have been recent examples of wave energy concepts being tested in the laboratory environment. One such experiment was conducted where a WEC's hydrodynamic properties (inertia and resonant frequency) were simulated through the use of a U-tube, partially water-filled, with the intention of testing a PTO system [7]. An irregular time varying pressure was applied at one end of the tube with the resulting pressure at the other end reacting against the PTO. The pressure was defined to consist of the excitation and radiation damping forces. The main findings of the work were that the PTO and control algorithms could be inexpensively tested; the U-tube geometry and time-varying pressure needed to meet specific constraints for adequate simulation; the validity of the approach depends on the wave and body motion amplitudes being much smaller than the body's characteristic length; and that the technique adopted does not cater for non-linear flow effects around the WEC body [7].

A wave energy application that applies HIL to a tubular generator drive is presented in [8]. The main purpose of this work was to test the power conversion capabilities; and control algorithms of a tubular permanent magnet linear generator prototype. The generator was designed, constructed and tested to investigate its generating capabilities, although this was independent to any WEC dynamics. A rotary permanent magnet synchronous generator (PMSG) was used to emulate the linear generator and coupled to a permanent magnet synchronous motor (PMSM) such that the WEC

response to a monochromatic wave input could be emulated. The WEC was modelled as a single DoF, heaving semi-submerged sphere, where a complex-conjugate control strategy was adopted. The aim of this approach was to optimally match, in real-time, the load impedance to the intrinsic impedance of the WEC [8]. The real components under test included: the PMSG; the control hardware for the PMSG; and a power converter for driving the PMSG. The simulated components were: the real-time control hardware for computing the WEC dynamics; the PMSM; and a power inverter for driving the PMSM. The main outcome of the project was the establishment of a HIL test bench, suitable for control system development. Following analysis of the system response to monochromatic wave inputs it was claimed that the HIL results validated the theoretical control systems [8].

Another application that can be described as HIL is the emulation of a single degree-of-freedom WEC involving the use of a vernier hybrid machine (VHM) [9]. The WEC was modelled as a spring-mass-damper system where the VHM translator mass was used to represent the WEC mass in addition to providing the PTO functionality. The WEC stiffness and damping were represented by tension springs and test equipment friction respectively. The hydrodynamic parameters deriving from radiation damping were not included in the model and the excitation forces were modelled as monochromatic such that reactive (phase and amplitude) control could be tested. This application can be regarded as an example of HIL, as the physical WEC emulator feeds into the reactive control system, actuating the VHM. The main findings of the project were that reactive control allows higher power capture compared with no control for monochromatic excitation forces and that special attention is needed regarding the high peak to average power ratio when reactive control is used [9].

IV. HIL System Description

Fig. 1 shows the composition of the HIL system in terms of its real (white) and simulated (grey + dashed) components. Note that the distinction of real and simulated parts is not a distinction between hardware and software but rather which components exist on the real WECs and which are simulated or emulated processes. The excitation force generator provides the excitation forces for each floating body over the duration of the HIL simulation. These forces together with the PTO force feed into the hydrodynamic WEC model which then outputs the relative position of the two bodies. A detailed explanation of this model is given in Section VI.

An important consideration for HIL simulation is that the dynamics of the emulated system feedback into the simulated system, introducing effects that would not occur in reality. The non-linear dynamics of the hydraulics are related to oil pressure, oil flow, hose friction, valve operation, accumulator expansion / contraction and oil compressibility. It is desirable to cancel these dynamics in the simulation if possible; however in the current context such dynamics are very fast compared to those of the WEC model and were therefore neglected for this project.

Emulation of the WEC motion is implemented using a hydraulic power pack, controlled using set point tracking of the PTO relative position. The inner loop of Fig. 1 shows the implementation of this. It was chosen to track the position rather than velocity or acceleration to avoid numerical inaccuracies causing over-excursions, potentially damaging the test-rig. The PTO force closes the HIL loop where a force sensor feeds back the measured force into the WEC model, running on the real-time embedded microcontroller.

A proportional flow control valve, installed into the power pack, controls oil flow through the driving cylinder using built in position feedback on the valve spool. Deadband is a property of the valve and restricts flow until approximately +/- 20% of the control command range has been exceeded. A look-up-table (LUT) has been used to overcome this deadband and linearise the valve while mapping the desired relative WEC velocities to valve flow rates. This mapping was determined through open-loop experiments where WEC velocities were measured following a series of directly actuated valve commands. The input to the valve controller is a +/- 10V set point command from the microcontroller.

The proportional flow control valve connects directly to the driving cylinder that drives against the resisting force of the PTO cylinder. The WEC's relative velocity is measured in real-time and fed back to the relative position control loop via an analog-to-digital converter (ADC), software integrator and negative feedback. The ADC and integrator are implemented internally by the position sensor's signal amplifier unit.

The excitation forces, generated offline, dictate the duration of the HIL simulation and are obtained using the following procedure:

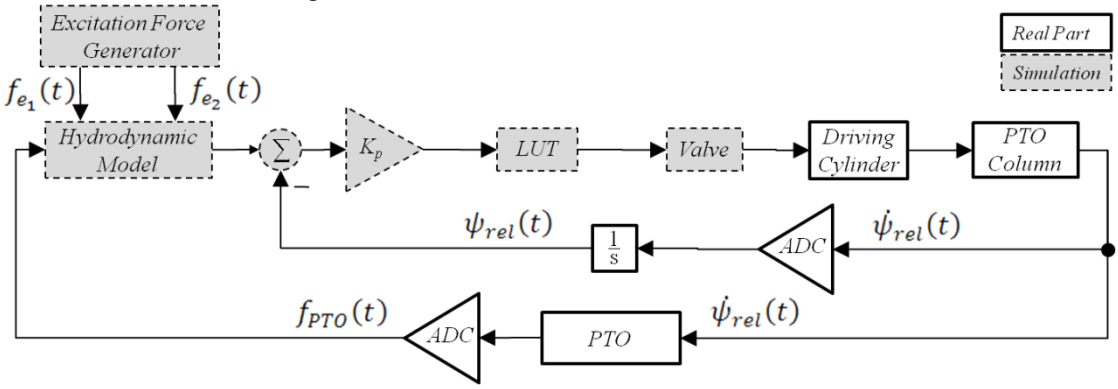

Fig. 1 HIL Architecture

1) Use the spectral distribution [1], expressed in equations (1) to (4), to obtain the wave elevation amplitudes for each frequency of the desired sea-state;

$$S(\omega) = 320\frac{H_s^2}{T_p^4}\omega^{-5}\exp\left(\frac{-1950}{T_p^4}\omega^{-4}\right)\cdot\gamma^Y, \quad (1)$$

where:

$$Y = \exp\left(-\left(\frac{\frac{\omega T_p}{2\pi}-1}{\sigma\sqrt{2}}\right)^2\right), \quad (2)$$

$$\sigma = \begin{cases} 0.07 & \text{for } \omega \le 2\pi T_p^{-1} \\ 0.09 & \text{for } \omega > 2\pi T_p^{-1} \end{cases} \quad (3)$$

$$\text{and } A_k = \sqrt{2S(\omega_k)d\omega} \quad (4)$$

2) For each frequency, calculate the excitation force amplitudes and phases. This is typically done using transfer functions obtained from radiation/diffraction panel software such as WAMIT ©. These transfer functions provide frequency dependent scaling relationship for each wave elevation amplitude and associated phases of each wave elevation frequency component;

3) For each frequency of the wave elevation, add a random phase to those obtained using the transfer function;

4) Construct the excitation force time-series by superimposing each cosine frequency component.

Note that the two WEC bodies have independent excitation forces and so the above process is done twice. Note that the WAFO toolbox [10] for MATLAB ® was used to obtain JONSWAP spectral distributions given the values of H_s, T_p and γ.

V. PTO System

To validate the HIL approach, we used a representative PTO comprising a hydraulic cylinder connected to a motorised proportional valve instead of a real PTO (shown in Fig. 3). This PTO was used primarily as it exhibits a reasonably linear characteristic for several valve settings close to the mid range point. This makes it compatible for comparison with ideal linear damping results from computer simulations.

The main components of the PTO are the hydraulic PTO cylinder operating in the vertical plane ('CYL1' in Fig. 3) and a motorised proportional valve ('OR3' in Fig. 3) that varies the PTO damping coefficient. This valve is operated offline and held constant during the HIL simulations using the device's independent internal feedback control. The combination of this control feature and offline characterisation experiments facilitated operation of the valve in its most linear region with good repeatability. The force sensor (see Fig. 2) connects the PTO cylinder piston rod to the PTO column which is connected to the driving cylinder piston rod. Stroke is limited using buffers end stops, mounted at the top and bottom of the PTO column. A position sensor mounted to the lower buffer assembly provides position feedback as the PTO column moves in the vertical plane.

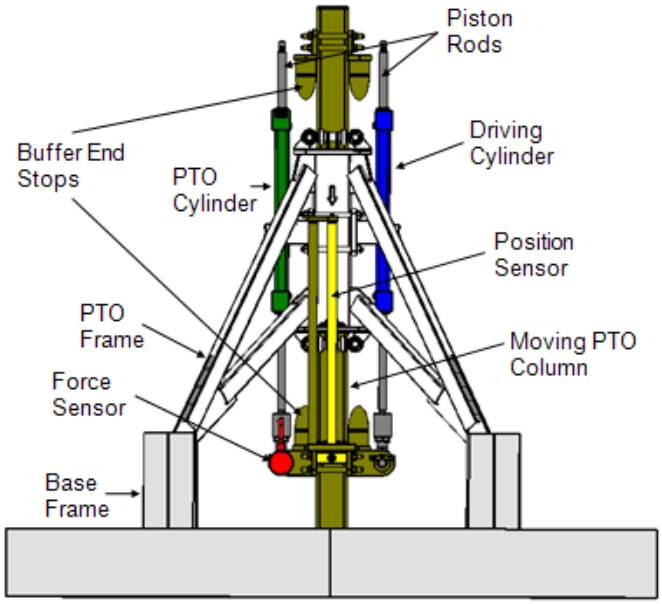

Fig. 2 HIL Test-Rig Schematic

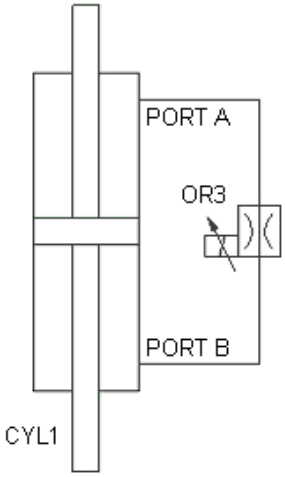

Fig. 3 PTO Cylinder and Proportional Valve Schematic

Fig. 4 Hardware-in-the-Loop Test-Rig

VI. WEC MODEL

The WEC has been modelled as a heave-only, two-body, linear time-invariant (LTI) system. The equations of motion for this WEC are [11]:

$$\begin{aligned}(m_1 + a_{\infty_{11}})\ddot{\psi}_1(t) + a_{\infty_{12}}\ddot{\psi}_2(t) \\ + \int_{-\infty}^{t} L_{11}(t-\tau)\dot{\psi}_1(t)d\tau \; + \\ + \int_{-\infty}^{t} L_{12}(t-\tau)\dot{\psi}_2(t)d\tau + c_1\psi_1(t) = f_{e_1}(t) + f_{PTO}(t)\end{aligned} \tag{5}$$

$$\begin{aligned}(m_2 + a_{\infty_{22}})\ddot{\psi}_2(t) + a_{\infty_{21}}\ddot{\psi}_1(t) \\ + \int_{-\infty}^{t} L_{21}(t-\tau)\dot{\psi}_1(t)d\tau \; + \\ + \int_{-\infty}^{t} L_{22}(t-\tau)\dot{\psi}_2(t)d\tau + c_2\psi_2(t) = f_{e_2}(t) - f_{PTO}(t)\end{aligned} \tag{6}$$

$$\psi_{rel}(t) = \psi_1(t) - \psi_2(t) \tag{7}$$

The convolution integral terms above represent the radiation damping forces acting on the WEC. Calculating these in real-time is computationally intensive on typical microcontrollers. An approximation technique has been implemented here to ensure computational efficiency on the microcontroller, executing at a sample rate of 10mS. There are a few techniques in the literature to approximate the convolution integral, both in the time [12],[13] and frequency domains [13]. In this paper we develop a state-space model derived from impulse response functions $L(t)$, based on the work from Duclos *et al.* [14]. This technique is called Prony's method which approximates a continuous function as a series of complex damped sinusoids. This can be expressed as [15]:

$$\hat{L}(t) = \mathrm{Re}\left\{\sum_{i=1}^{Q} \beta_i e^{\alpha_i t}\right\} = \sum_{i=1}^{Q} \hat{L}_i(t) \tag{8}$$

where the Prony parameters are defined as:

$$\beta_i \triangleq \beta_{a_i} + j\beta_{b_i} \tag{9}$$

$$\alpha_i \triangleq \alpha_{a_i} + j\alpha_{b_i} \tag{10}$$

with $\beta_i, \alpha_i \in \mathbb{C}$, $\beta_{a_i}, \beta_{b_i}, \alpha_{a_i}, \alpha_{b_i} \in \mathbb{R}$ and $j^2 = -1$. Observation of Euler's formula shows that each element of the sum in (8) is equivalent to:

$$\hat{L}_i(t) = \beta_{a_i} e^{\alpha_{a_i} t}\cos(\alpha_{b_i} t) - \beta_{b_i} e^{\alpha_{a_i} t}\sin(\alpha_{b_i} t) \tag{11}$$

The Prony parameters β_i and α_i can be obtained using the procedure in the appendix of [14]. The order of the approximation Q, is determined manually based on a compromise between accuracy of fit and the computational efficiency of the convolution integral at run-time. Also, each complex damped sinusoid needs to be stable, requiring α_{a_i} to be negative. Hence any solutions of $\hat{L}_i$ with a positive value of α_{a_i} must be removed from the approximation.

The solution of $\hat{L}(t)$ can be composed of couples of complex conjugate exponentials and/or single real exponentials [14]. For the complex conjugate pairs only one of the pair is needed with its amplitude scaled by 2 to account for the other pair. In this case:

$$\hat{L}_i(t) = 2\beta_{a_i} e^{\alpha_{a_i} t}\cos(\alpha_{b_i} t) - 2\beta_{b_i} e^{\alpha_{a_i} t}\sin(\alpha_{b_i} t) \tag{12}$$

In the case of real exponentials:

$$\hat{L}_i(t) = \beta_{a_i} e^{\alpha_{a_i} t} \tag{13}$$

With the Prony parameters, the convolution integrals may be constructed into state space LTI subsystems such that they fit into an overall state space structure of the WEC model. The state space representation of the convolution integrals associated with WEC 'body-*b*' can be expressed as [12]:

$$\dot{\mathbf{X}}_{\mathrm{C}}(t) = \mathbf{A}_{\mathrm{C}}\mathbf{X}_{\mathrm{C}}(t) + \mathbf{B}_{\mathrm{C}} v_b(t) \tag{14}$$

$$y_C(t) = \mathbf{C}_{\mathrm{C}}\mathbf{X}_{\mathrm{C}}(t) \approx \int_{-\infty}^{t} L(t-\tau) v_b(t) d\tau \tag{15}$$

This state space system is constructed with sub-subsystems for each component $\hat{L}_i$, built using the Prony parameters. The idea behind this transformation is that we can find a transfer function $G(s)$ such that $G(s) = \mathcal{L}(L(t))$. Firstly, the case of complex conjugate pairs is presented. To simplify the algebraic manipulation, (12) is transformed into the frequency domain using the Laplace transform [16] and multiplied by the input, $V_b(s)$, to form the *i*-th component of the convolution integral approximation as:

$$\begin{aligned}Y_{C_i}(s) &= G_{C_i}(s)V_b(s) \\ &= \frac{2\beta_{a_i}s - 2\beta_{a_i}\alpha_{a_i} - 2\beta_{b_i}\alpha_{b_i}}{s^2 - 2\alpha_{a_i}s + \alpha_{a_i}^2 + \alpha_{b_i}^2} \cdot V_b(s)\end{aligned} \tag{16}$$

Taking the inverse Laplace transform of (16) and defining the following variables:

$$\begin{aligned}\dot{x}_{1c_i}(t) \triangleq \left(-\alpha_{a_i}^2 - \alpha_{b_i}^2\right)y_{C_i}(t) \\ + \left(-2\beta_{a_i}\alpha_{a_i} - 2\beta_{b_i}\alpha_{b_i}\right)v_b(t)\end{aligned} \tag{17}$$

$$x_{2c_i}(t) \triangleq y_{C_i}(t) \tag{18}$$

yields:

$$\dot{y}_{C_i}(t) = x_{1c_i}(t) + 2\alpha_{a_i}y_{C_i}(t) + 2\beta_{a_i}v_b(t) \tag{19}$$

The resulting state space form of the sub-subsystem is then:

$$\begin{aligned}\begin{bmatrix}\dot{x}_{1c_i}(t) \\ \dot{x}_{2c_i}(t)\end{bmatrix} &= \begin{bmatrix}0 & -\alpha_{a_i}^2 - \alpha_{b_i}^2 \\ 1 & 2\alpha_{a_i}\end{bmatrix}\begin{bmatrix}x_{1c_i}(t) \\ x_{2c_i}(t)\end{bmatrix} \\ &+ \begin{bmatrix}-2\beta_{a_i}\alpha_{a_i} - 2\beta_{b_i}\alpha_{b_i} \\ 2\beta_{a_i}\end{bmatrix}v_b(t)\end{aligned} \tag{20}$$

$$y_{C_i}(t) = \begin{bmatrix}0 & 1\end{bmatrix}\begin{bmatrix}x_{1c_i}(t) \\ x_{2c_i}(t)\end{bmatrix} \tag{21}$$

For the case of real exponentials (13) is transformed to the frequency domain, again using standard Laplace tables, and multiplied by $V_b(s)$ to give:

$$Y_{C_i}(s) = \frac{\beta_{a_i}}{s - \alpha_{a_i}}V_b(s) \tag{22}$$

Converting this back to the time domain in a form that facilitates the construction of a state space model gives:

$$\dot{y}_{C_i}(t) = \alpha_{a_i}y_{C_i}(t) + \beta_{a_i}v_b(t) \tag{23}$$

The resulting state space subsystem is therefore:

$$[\dot{x}_{1c_i}(t)] = [\alpha_{a_i}][x_{1c_i}(t)] + [\beta_{a_i}]v_b(t) \tag{24}$$

$$y_{C_i}(t) = [1][x_{1c_i}(t)] \tag{25}$$

The matrices $\mathbf{A}_C, \mathbf{B}_C$ and $\mathbf{C}_C$, are finally constructed from the above state space sub-systems as follows.

$$\mathbf{A}_C = \begin{bmatrix} \mathbf{\Lambda}_1 & & \mathbf{0} \\ & \ddots & \\ \mathbf{0} & & \mathbf{\Lambda}_Q \end{bmatrix} \tag{26}$$

$$\mathbf{B}_C = \begin{bmatrix} \mathbf{P}_1 \\ \vdots \\ \mathbf{P}_Q \end{bmatrix} \tag{27}$$

$$\mathbf{C}_C = [\mathbf{E}_1 \quad \dots \quad \mathbf{E}_Q]$$

where:

$$\mathbf{\Lambda}_i = \begin{cases} [\alpha_{a_i}] & \text{for } \alpha_{b_i} = 0, \\ \begin{bmatrix} 0 & -\alpha_{a_i}^2 - \alpha_{b_i}^2 \\ 1 & 2\alpha_{a_i} \end{bmatrix} & \text{otherwise.} \end{cases} \tag{28}$$

$$\mathbf{P}_i = \begin{cases} [\beta_{a_i}] & \text{for } \alpha_{b_i} = 0, \\ \begin{bmatrix} -2\beta_{a_i}\alpha_{a_i} - 2\beta_{b_i}\alpha_{b_i} \\ 2\beta_{a_i} \end{bmatrix} & \text{otherwise.} \end{cases} \tag{29}$$

$$\mathbf{E}_i = \begin{cases} [1] & \text{for } \alpha_{b_i} = 0, \\ [0 \quad 1] & \text{otherwise} \end{cases} \tag{30}$$

Assembling all four convolution integral subsystems with the remaining terms of (5), (6) and (7) gives the following state space system:

$$\dot{\mathbf{X}}(t) = \mathbf{A}\mathbf{X}(t) + \mathbf{B}\mathbf{F}(t) \tag{31}$$

$$y(t) = \mathbf{C}\mathbf{X}(t) + \mathbf{D}\mathbf{F}(t) \tag{32}$$

where:

$$\mathbf{A} = \left[\begin{array}{cc|cccc} \mathbf{0} & \mathbf{M'K} & \mathbf{M'} & \begin{bmatrix} \mathbf{C}_{C_1} & \mathbf{C}_{C_2} & \mathbf{0} & \mathbf{0} \\ \mathbf{0} & \mathbf{0} & \mathbf{C}_{C_3} & \mathbf{C}_{C_4} \end{bmatrix} \\ \mathbf{I} & \mathbf{0} & & \begin{matrix} \mathbf{0} & \mathbf{0} & \mathbf{0} & \mathbf{0} \\ \mathbf{0} & \mathbf{0} & \mathbf{0} & \mathbf{0} \end{matrix} \\ \hline \mathbf{B}_{C_1} & \mathbf{0} \quad \mathbf{0} \quad \mathbf{0} & \mathbf{A}_{C_1} & & \mathbf{0} & \\ \mathbf{0} & \mathbf{B}_{C_2} \quad \mathbf{0} \quad \mathbf{0} & & \mathbf{A}_{C_2} & & \\ \mathbf{B}_{C_3} & \mathbf{0} \quad \mathbf{0} \quad \mathbf{0} & & & \mathbf{A}_{C_3} & \\ \mathbf{0} & \mathbf{B}_{C_4} \quad \mathbf{0} \quad \mathbf{0} & \mathbf{0} & & & \mathbf{A}_{C_4} \end{array}\right] \tag{33}$$

$$\mathbf{B} = \begin{bmatrix} \mathbf{M}^{-1} \\ \mathbf{0} \\ \vdots \\ \mathbf{0} \end{bmatrix}, \mathbf{C} = [0 \quad 0 \quad 1 \quad -1 \quad 0 \quad \dots \quad 0], \mathbf{D} = [0 \quad 0],$$

$$\mathbf{M} = \begin{bmatrix} m_1 + a_{\infty_{11}} & a_{\infty_{12}} \\ a_{\infty_{21}} & m_2 + a_{\infty_{22}} \end{bmatrix}, \mathbf{M'} = -\mathbf{M}^{-1},$$

$$\mathbf{F}(t) = \begin{bmatrix} f_{e_1}(t) + f_{PTO}(t) \\ f_{e_2}(t) - f_{PTO}(t) \end{bmatrix}, \mathbf{I} = \begin{bmatrix} 1 & 0 \\ 0 & 1 \end{bmatrix}, \mathbf{K} = \begin{bmatrix} c_1 & 0 \\ 0 & c_2 \end{bmatrix}$$

$$\mathbf{X} = \begin{bmatrix} x_1 & x_2 & x_3 & x_4 & [\mathbf{X}_{C_1}]^T & [\mathbf{X}_{C_2}]^T & [\mathbf{X}_{C_3}]^T & [\mathbf{X}_{C_4}]^T \end{bmatrix}^T$$

Note that in (33) the sub-subscripts 1 to 4 correspond to the subsystem approximations associated with $L_{11}(t)$, $L_{12}(t)$, $L_{21}(t)$ and $L_{22}(t)$ respectively.

VII. HARDWARE & SOFTWARE ARCHITECTURE

Fig. 5 shows the subsystem interaction of the HIL test simulator consisting of the operator station, the test-rig and the prime mover (or hydraulic power pack). Single-phase AC provides power to the operator control station consisting of a computer, WiFi router and DC power supply unit (PSU). The PSU supplies all components of the test-rig and the power pack except the motor / pump unit which is supplied by a three-phase AC outlet.

Fig. 6 shows the interaction between the three main software layers used of the HIL system. Note that each layer executes independently. The highest layer runs on the host machine and is responsible for user interaction of set point control, sensor monitoring, transfer of logged data and post processing. The real-time code runs on a National Instruments Compact-RIO (cRIO), a stand-alone programmable-automation controller (PAC) that performs the core functionality of the HIL system including the WEC simulation, power pack control, damping coefficient control, data acquisition, and input-output (I/O) interfacing to the field-programmable-gate-array (FPGA) layer. The cRIO communicates with the host machine through a WiFi module mounted in one of its I/O slots. The FPGA layer connects the real-time code to the sensors and actuators of the test-rig.

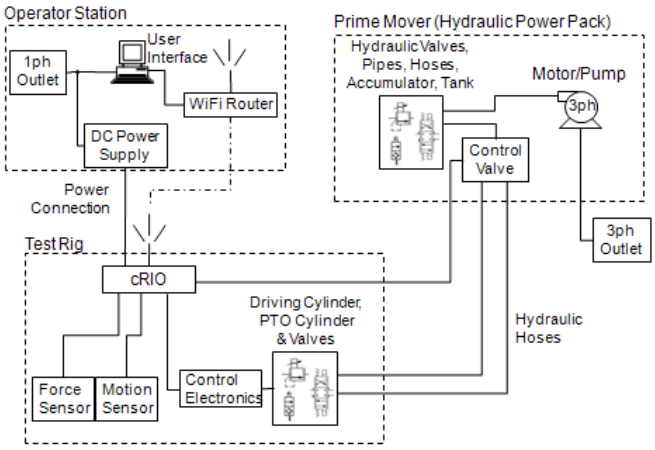

Fig. 5 Instrumentation Diagram of HIL Simulator

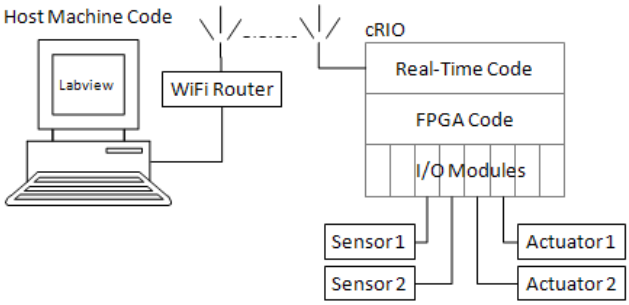

Fig. 6 Software Layer Architecture

The WEC simulation is implemented using built-in Labview matrix algebra functions to solve the state space system defined by discretised versions of (31) and (32) using the zero-order-hold (ZOH) method. Note that the state space system is discretised offline to remove the necessity of integrating the state variables at each time step, thus improving computational efficiency. The excitation forces obtained offline are added to the real-time measured PTO force and fed in to the state space model, producing a real-time relative position that is provided as a set point to the position control loop.

The HIL simulations were run for two damping coefficients of interest, corresponding to: the minimum possible damping on the test-rig (D_1 in Table 1); and the most linear region of the valve (D_2 in Table 1). In each case comparisons were made with computer simulations where each simulation has been given the following designations:

TABLE I
HIL AND COMPUTER SIMULATION DESIGNATIONS

Damping Coefficient	HIL Simulation	Computer Simulation
D_1	HIL1	Sim1
$D_2 = 4D_1$	HIL2	Sim2

The HIL1 and HIL2 simulations both ran successfully, correlating well to Sim1 and Sim2 respectively, the results of which are provided in the following section.

VIII. RESULTS

A. Validation

Prior to running any hardware tests the following validation stages were carried out:

1) Validation of the continuous state space model, based on a Prony approximation with $Q = 5$ for all impulse responses, compared to a previously developed, non-state space model;

2) Validation of the discrete state space model in the real-time environment.

Fig.'s 7 and 8 show these results respectively. Note the slight differences in system responses of Fig. 7. These arise due to the fact that the impulse response functions and convolution integrals for the state space model are approximations of those used in the other model. It is considered that the discrepancy is within reasonable limits.

B. PTO Characterisation

Measurements of the PTO force and velocity were carried out to obtain the PTO characteristics, where sinusoidal motion was applied to the PTO using the hydraulic power pack. Fig.'s 9 and 10 show the results, displaying the relationship between the PTO forces and velocities for the HIL2 and HIL1 cases respectively. The first observation is that there exists a discontinuity in the force around the zero velocity axis. One feature is the positive and negative bias in the force for negative and positive velocities respectively.

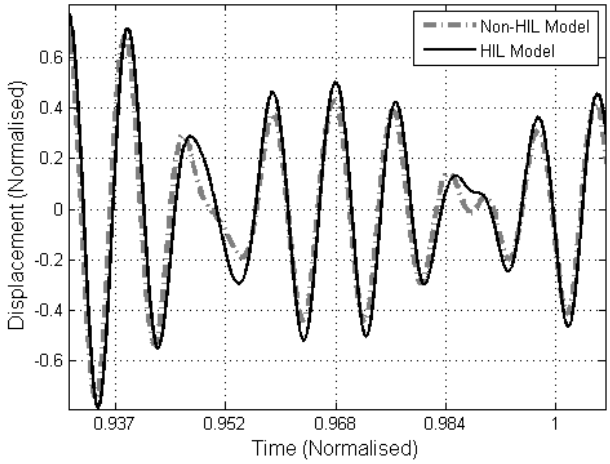

Fig. 7 Validation of Continuous State Space Model

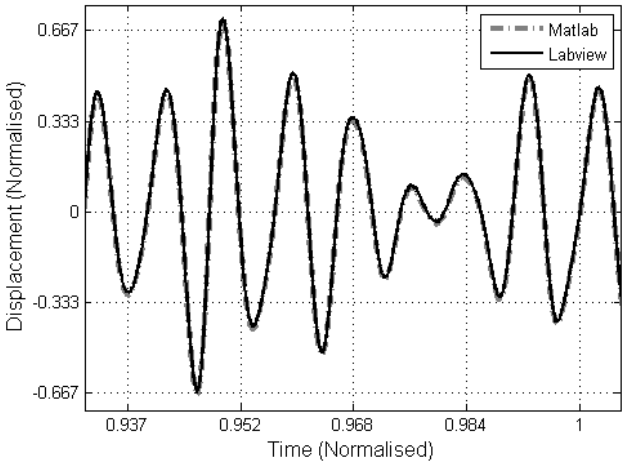

Fig. 8 Validation of Real-Time Discrete State Space Model (HIL2)

This is obviously not expected from the ideal linear damping case, which would be a straight line through zero. Examination showed this feature to be caused by cylinder seal friction. The second feature that can be observed is a uniform bias that shifts all points in the positive direction. This was found to be caused by the weight of the cylinder rods. Another observation from these results is that away from the zero-velocity region the PTO behaves reasonably linearly for both HIL1 and HIL2 cases, although with less scatter for HIL2. Several experiments with a variety of damping coefficients showed that the force-velocity relationship was not always linear although this tended to be more the case towards the extreme case of a fully closed PTO valve. This highlights an important advantage of HIL testing: that is the ability to capture unmodeled features of a real system that would not necessarily be detected in computer simulations.

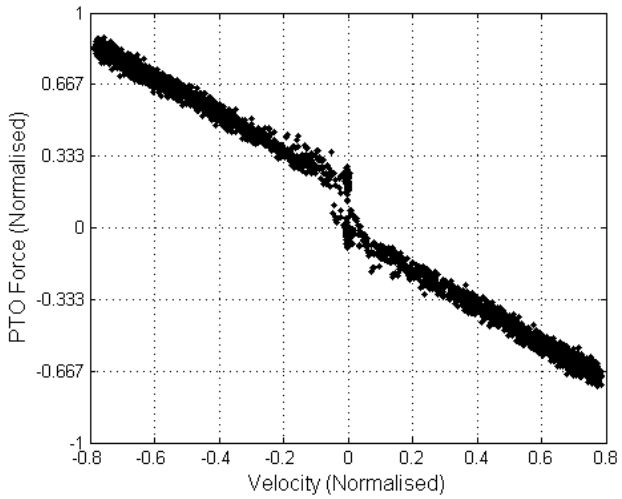

Fig. 9 PTO Characterisation Data for HIL2

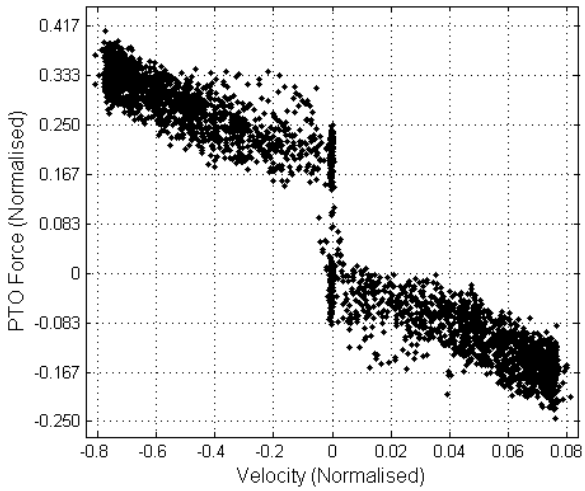

Fig. 10 PTO Characterisation Data for HIL1

Fig. 11 shows the results of the characterisation tests carried out on the power pack control valve. The main point of interest here is the deadband region of the valve for a significant proportion of the valve's operating region around zero. A nonlinear relationship can also be seen for all velocities. This measured characteristic was used to cancel the nonlinearities using the LUT previously described. Independent LUTs were created for HIL1 and HIL2.

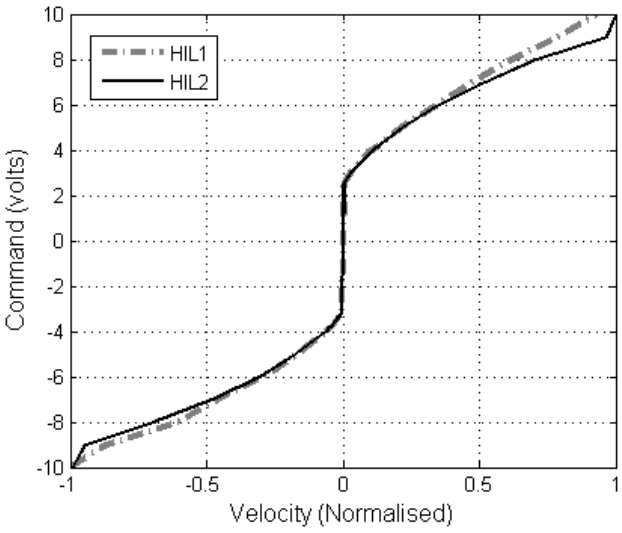

Fig. 11 Power Pack Control Valve Characteristic

C. Comparison of HIL and Computer Simulations

Fig.'s 12 and 13 show the comparisons between the HIL2/HIL1 and Sim2/Sim1 results respectively. The following observations have been made:

- There is a reasonably close correlation between the two responses;
- There is a noticeable offset between the two responses;
- The correlation is good for high velocities and less so for low velocities.

Most importantly, the first observation confirms that the HIL simulation has performed satisfactorily. Regarding the second observation, analysis suggests this offset to be caused by the uniform offset in the PTO characteristic, again due to the asymmetric load of the cylinder rod masses. The third observation shows how the discontinuity at zero velocity in the PTO characteristic leads to a significant departure from expected results of the linear computer simulation for low velocities.

The discrepancies between 'HIL' and 'Sim' results are due the inclusion of hardware into the loop, not surprising as the simplifying assumptions associated with the PTO have been removed. It should be noted that it is desirable to see some of these discrepancies in the output so that more realistic system behaviour can be identified prior to sea deployment. For example, the discontinuity of the PTO force around the zero-velocity region is a property of the real hardware under test, (friction in this case) and should not be cancelled out of the HIL loop as this provides insight into the system behaviour as it would be in reality. However, some discrepancies are undesirable as they are caused by the nature of the emulator and should ideally be cancelled out of the simulation. For example, in this project, a significant difference from reality is the fact that the PTO column is not attached to the centre buoy (immersed in water) and therefore not supported by buoyancy as would be the case in reality. This causes the weight of the cylinder rods to bias the PTO force. It is therefore valid to cancel this effect in the simulation.

IX. CONCLUSION

Hardware-in-the-loop has been successfully implemented and tested on a scale model of a heave-only, two-body, point-absorber WEC. This is the first time in the wave energy industry, known to the authors, that HIL has been implemented to such a level of detail on an actual scale model capable of experiments at sea.

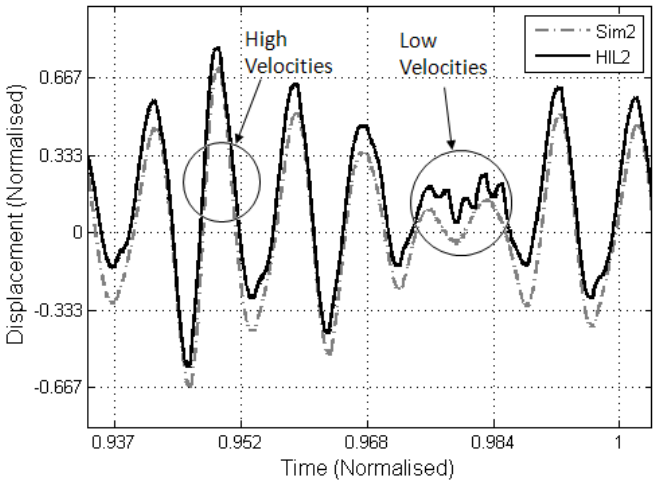

Fig. 12 Comparison of HIL2 and Sim2

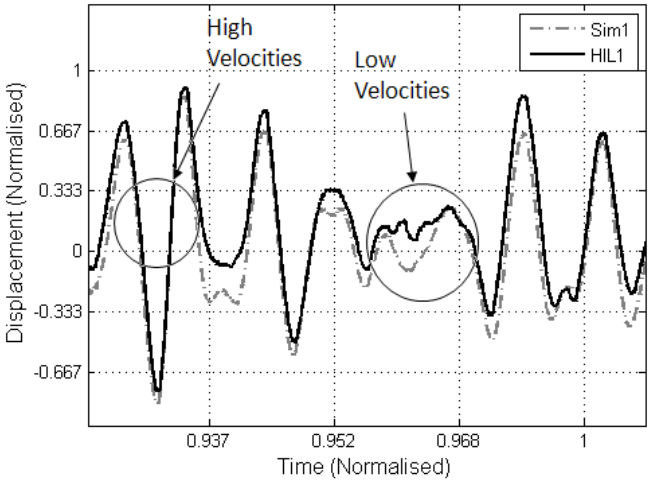

Fig. 13 Comparison of HIL1 and Sim1

The WEC was modelled as a state space LTI system using Prony's method in the approximation of the four convolution integral terms. This model was validated against an alternative non-state space model using the traditional method of calculating the convolution integral. The state space model allowed a real-time sample period of 10mS to be used.

Close correlation was observed between the HIL and computer simulations, with two main differences in the output response. One of these was a consequence of the emulator's physical properties feeding back into the simulation whereas the other was due to a property of the real PTO under test. These results highlight an important consideration with HIL simulations which is the need to cancel dominant properties (static and dynamic) of the emulator such that they do not influence the HIL simulation. The results also demonstrate how HIL simulations allow for the discovery of system behaviour that would otherwise be left undetected in computer simulations due to simplified assumptions.

ACKNOWLEDGMENTS

This work was partly funded by the European Community's Seventh Framework Programme (FP7/2007-2013) under grant agreement n° 239376 (STANDPOINT Project). The first author wishes to acknowledge Wavebob management for providing access to the scale WEC test rig and allowing it to be modified for the purposes of this study within the framework of his M.Eng degree.

REFERENCES

[1] J.M.J. Journée, and W.W. Massie, *Offshore Hydromechanics*, 1st Ed., Delft University of Technology, 2001.

[2] R. Isermann, J. Schaffnit, and S. Sinsel, "Hardware-in-the-loop simulation for the design and testing of engine-control systems" *Control Engineering Practice*, Vol. 7, No. 5, pp. 643-653, May. 1999.

[3] P. Terwiesch, T. Keller, and E. Scheiben, "Rail vehicle control system integration testing using digital hardware-in-the-loop simulation" *IEEE Transactions on Control Systems Technology*, Vol. 7, No. 3, pp. 352-362, May. 1999.

[4] J. de Carufel, E. Martin, and J. C. Piedboeuf, "Control strategies for hardware-in-the-loop simulation of flexible space robots" *IEE Proceedings - Control Theory and Applications*, Vol. 147, No. 6, pp. 569-579, Nov. 2000.

[5] A. Ganguli, A. Deraemaeker, M. Horodinca, and A. Preumont, "Active damping of chatter in machine tools – demonstration with a 'hardware-in-the-loop' simulator" *Proceedings of the Institution of Mechanical Engineers, Part I: Journal of Systems and Control Engineering*, Vol. 219, No. 5, pp. 359-369, Mar. 2005.

[6] H. Li, M. Steurer, K. L. Shi, S. Woodruff, and D. Zhang, "Development of a unified design, test, and research platform for wind energy systems based on hardware-in-the-loop real-time simulation" *IEEE Transactions on Industrial Electronics*, Vol. 53, No. 4, pp. 1144-1151, Aug. 2006.

[7] A. F. de O. Falcão, P.E.R. Pereira, J.C.C. Henriques, and L.M.C. Gato, "Hydrodynamic simulation of a floating wave energy converter by a U-tube rig for power take-off testing" *Ocean Engineering*, Vol. 37, No. 14-15, pp. 1253-1260, Oct. 2010

[8] V. Delli Colli, P. Cancelliere, F. Marignetti, R. Di Stefano, and M. Scarano, "A tubular generator for marine energy direct drive applications" *IEEE Transactions on Industrial Electronics*, Vol. 53, No. 4, pp. 1473–1478, Aug. 2006.

[9] J.K.H. Shek, D.E. Macpherson, M.A. Mueller, "Phase and amplitude control of a linear generator for wave energy conversion", *4th IET Conference on Power Electronics, Machines and Drives (PEMD 2008)*, 2008, pp. 66-70.

[10] P.A. Brodtkorb, P. Johannesson, G. Lindgren, I. Rychlik, J. Rydén, E. Sjö, "WAFO - a Matlab toolbox for analysis of random waves and loads", *Proceedings of the 10th International Offshore and Polar Engineering Conference*, 2000, Seattle, USA, Vol III, pp. 343-350.

[11] J. J. Cândido, and J. A. P. Justino, "Frequency, stochastic and time domain models for an articulated wave power device", *Proceedings of the ASME 27th International Conference on Offshore Mechanics and Arctic Engineering (OMAE2008)*, 2008, paper OMAE2008-57253, pp. 633-643.

[12] Z. Yu, and J. Falnes, "State-space modelling of a vertical cylinder in heave" *Applied Ocean Research*, Vol. 17, No. 5, pp. 265-275, Oct. 1995.

[13] T. Pérez, and T. I. Fossen, "Time vs frequency-domain identification of parametric radiation force models for marine structures at zero speed", *Modeling, Identification and Control*, Vol. 29, No. 1, pp. 1-19, Jan. 2008.

[14] G. Duclos, A. H. Clément, and G. Chatry "Absorption of outgoing waves in a numerical wave tank using a self-adaptive boundary condition", *International Journal of Offshore and Polar Engineering*, Vol. 11, No. 2, pp. 104-111, Jun 2001.

[15] L. Weiss, and R. N. McDonough, "Prony's method, z-transforms and padé approximation", *SIAM Review*, Vol. 5, No. 2, pp. 145-149, Apr. 1963.

[16] K. Ogata, *Modern Control Engineering*, 4th Ed., New Jersey, USA: Prentice Hall, 2002.